

Università degli Studi di Padova

---



Dipartimento di Fisica e Astronomia "Galileo Galilei"

Degree in Physics

Physics Laboratory report

## Timing

Author: **Luca Morselli**

Number: **1172019**

Author: **Andrea Raggio**

Number: **1178280**

Professors: **Francesco Recchia**  
**Luca Stevanato**

Academic Year 2017-2018

## Introduction

In particle detection one of the first and most important requirements is the production of a time reference for detected events. Correct definition of a particle detection time is essential to allow the production of coincidence signals between the different detectors which compose the arrays of an experimental set-up. Moreover the reduction of timing error is crucial for several measurements, such as the *Time of Flight* (TOF) technique, used to distinguish the particle type but also to measure its kinetic energy.

There are several ways to produce a timing reference for detected particles, the aim of a good technique is to increase the accuracy and reduce the dependence on particle energy (*Time walk*). The simplest one is the *Leading Edge* method, which associates the time reference of the signal with the crossing moment of a fixed threshold, for instance 0.2 as shown in Fig. 1-a. In scintillation detectors, where the rising time of the pulses is constant, this method is clearly affected by the amplitude of the signals, making it not good for the purpose. A better solution is the *Constant Fraction Discrimination* (CFD) technique (Fig. 1-b), which gives a time reference independent on pulse amplitude.

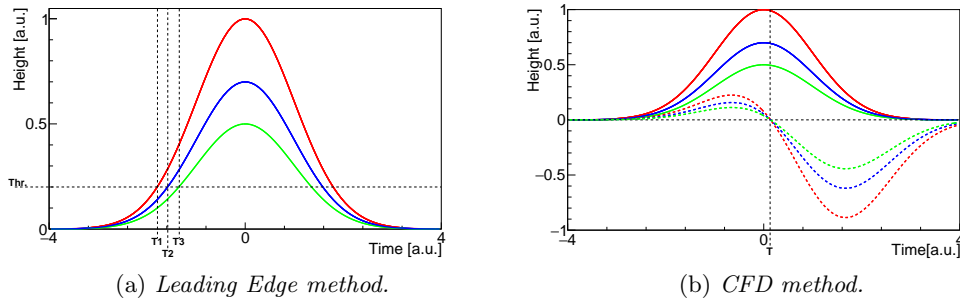


Figure 1: *Leading Edge* (a) and *Constant Fraction Discrimination* (CFD) (b) techniques applied on three Gaussian pulses with same mean and sigma but different amplitudes. The bipolar dashed pulses in b) are generated by the CFD algorithm.

The aim of this report is to present the timing analysis performed over two scintillation detectors. Therefore the following sections will analyze these steps:

- Energy calibration of the organic scintillators and calculation of the energy resolution from the analysis of the Compton edge.
- Optimization of the external delay of the analogue CFTD to obtain the best time resolution.
- Study the time resolution behaviour as a function of the energy.
- Comparison between the timing resolutions obtained from analogue and digital treatment of the signals.
- Measurement of the speed of light.

## Experimental Set Up

To perform the timing analysis two cylindrical organic scintillator EJ-228 with diameter and thickness of 5 cm were used, each one coupled with a Photonics Photomultiplier XP2020 (see Fig. 2). The anode outputs of the PMT were sent to a Quad Linear Gate FAN-IN/OUT mod. Philips 744 in order to split them. One output then was sent directly to a CAEN digitizer mod. DT5751, an ADC with a sampling rate of 1 Gs/s and a resolution of 10 bit, while the other one was sent to a Quad CFD mod. 935. The timing signals obtained from the CFD unit were processed by a CAEN Quad Logic Unit mod. N455 to produce a coincidence signal between the two detectors, used as trigger input for the digitizer. They were also sent to an Ortec TAC unit to measure their time difference. The output of the TAC module was also digitized.

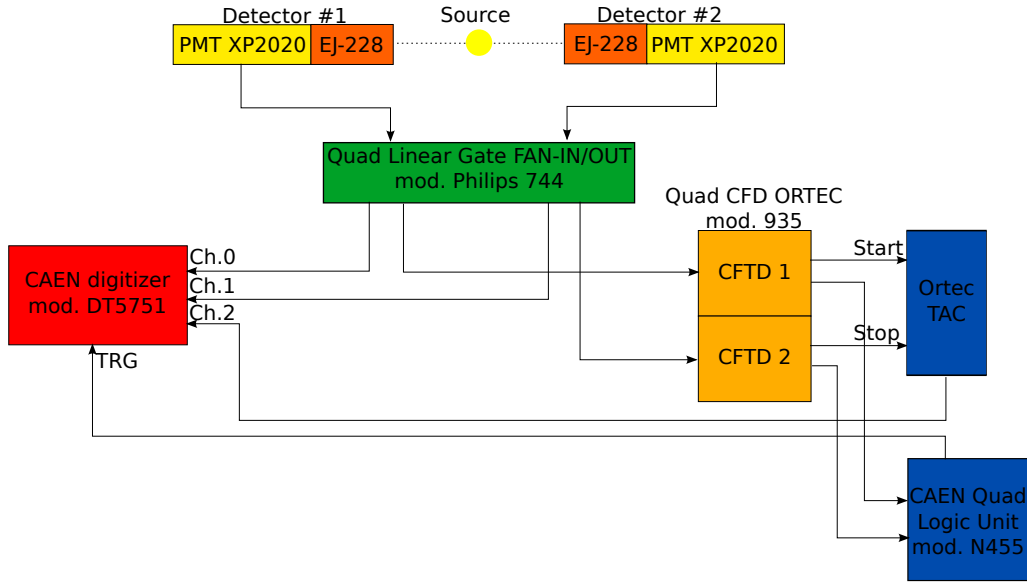


Figure 2: Experimental configuration adopted for the timing analysis.

## Energy Calibration

Due to the organic composition of our detectors the photo-electric cross-section of its constituents is negligible in the energy range considered. Furthermore total absorption through multiple Compton scattering is negligible too, because of detector limited size. The detectors response will be dominated by individual Compton interaction, thus the energy spectrum is a continuous distribution that corresponds to different angles of interaction. This can be seen in the spectra acquired with the  $^{22}\text{Na}$  source in Fig. 3.

The finite resolution of our detectors results in a shift towards lower energies depending on the detector resolution as shown in Fig. 4.

In order to obtain the energy calibration parameters, several smeared spectra were generated using the Klein-Nishina Compton Scattering cross-section (see Eq. 1) for 511 keV and 1275 keV  $\gamma$  respectively.

$$\frac{d\sigma}{dT} = \frac{\pi r_e^2}{m_e c^2 \alpha^2} \left( 2 + \frac{s^2}{\alpha^2 (1-s)^2} + \frac{s}{1-s} \left( s - \frac{2}{\alpha} \right) \right) \quad (1)$$

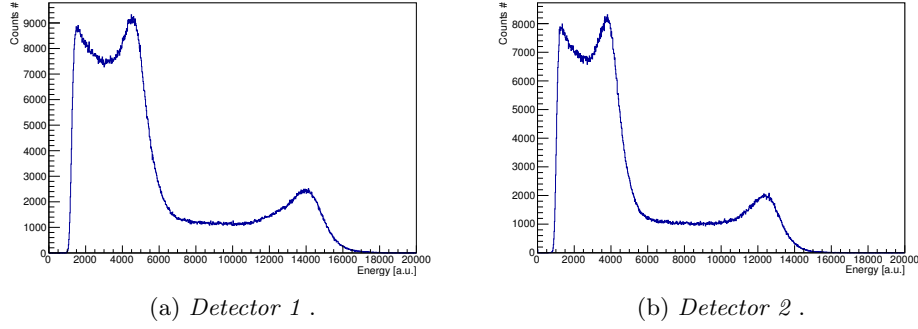


Figure 3: *Detector 1* (a) and *Detector 2* (b) uncalibrated energy spectra obtained from a  $^{22}\text{Na}$   $\gamma$  source.

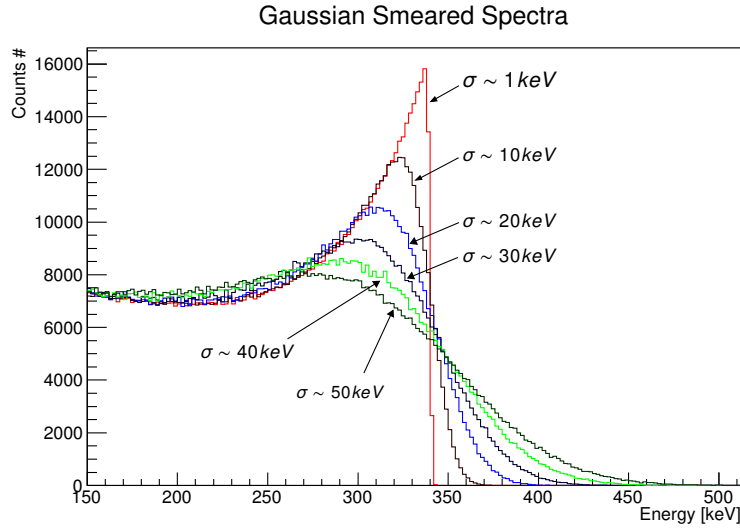


Figure 4: Gaussian smeared spectra at different  $\sigma$  generated using the Klein-Nishina Compton Scattering cross-section for 511 keV photons.

To locate the Compton edge then, the background from acquired spectra was removed as shown in Fig. 5. The  $\chi^2$  between experimental spectrum and Gaussian smeared spectra was minimized looping over different  $\sigma$  values. With the selected  $\sigma$  the corresponding shift of the Compton edge was computed in order to calibrate the detectors as shown in Tab. 1:

Detector	Photon Energy [keV]	$\sigma$ [keV]	C.E. shifting [keV]
1	511	34	40.66
	1275	40	52.15
2	511	28	34.66
	1275	40	52.15

Table 1:  $\sigma$  and C.E. shift for the two detectors.

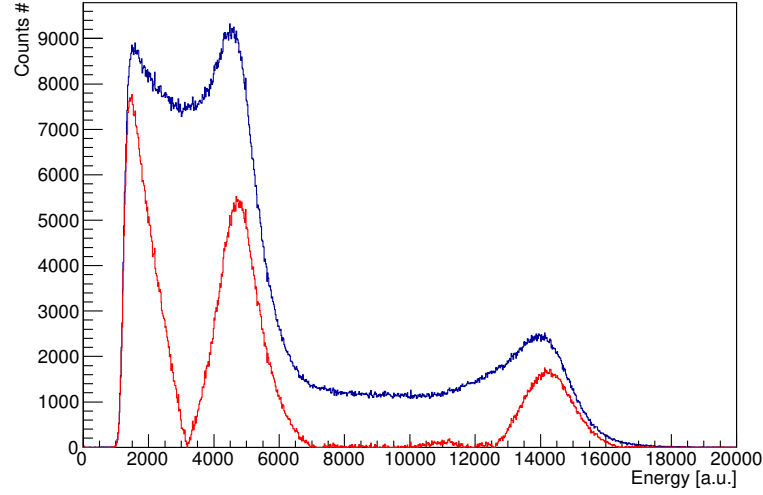
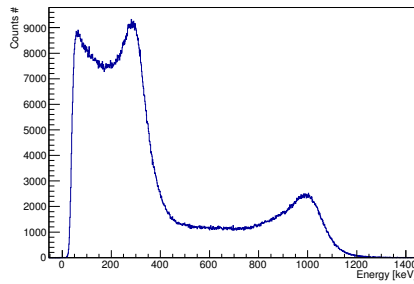


Figure 5:  $^{22}\text{Na}$  energy spectra. The blue one represent the original acquired spectrum, while the red one is obtained by background removal.

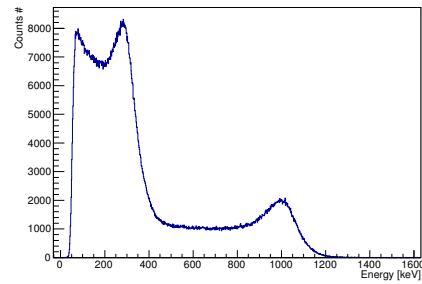
Finally the calibration parameters were computed (see Tab. 2), the  $^{22}\text{Na}$  calibrated spectra of the two detectors are shown in Fig. 6

Detector	a [keV/channel]	b [keV]
#1	$0.0748945 \pm$	$-54.2511 \pm$
#2	$0.083215 \pm$	$-32.6856 \pm$

Table 2: Calibration parameters.



(a) *Detector 1.*



(b) *Detector 2.*

Figure 6: *Detector 1* (a) and *Detector 2* (b) energy calibrated spectra obtained from a  $^{22}\text{Na}$   $\gamma$  source.

## TAC calibration

In order to calibrate the TAC unit, several spectra were produced using as start input the CFD timing signals and as stop the same signals delayed by a chosen value. With 2 ns delay steps the spectra of Fig. 7 was obtained, the peaks centroids were used to compute the calibration parameters performing a linear fit (see Fig. 8).

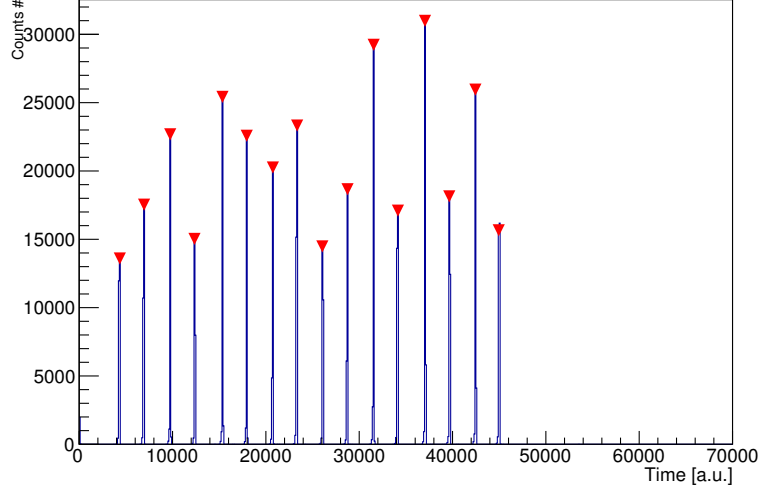
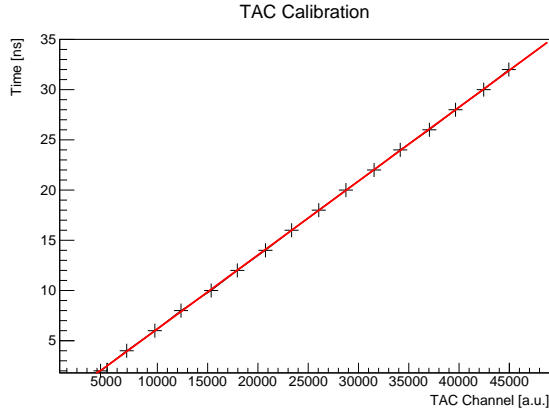


Figure 7: TAC uncalibrated spectrum obtained by an auto coincidence with 2 ns delay steps.



Parameter	Value
p0	$(-1.19 \pm 0.04) \text{ s}$
p1	$(7.36 \pm 0.01) \times 10^{-4} \text{ s/ch}$

Figure 8: Linear fit used to compute the TAC calibration parameters.

Fit parameters.

## External delay optimization

To produce the analog timing and measure its resolution the parameters of the CFD module needed to be optimized. The thresholds were set to reject events under  $\approx 30$  keV as show in the calibrated spectra of Fig. 6, while the CFD fraction is a fixed value chosen by the producer. The delay, finally, was selected performing test measurements with values in the range 3-6 ns, using the FWHM of timing distribution as resolution indicator as shown in Fig. 9.

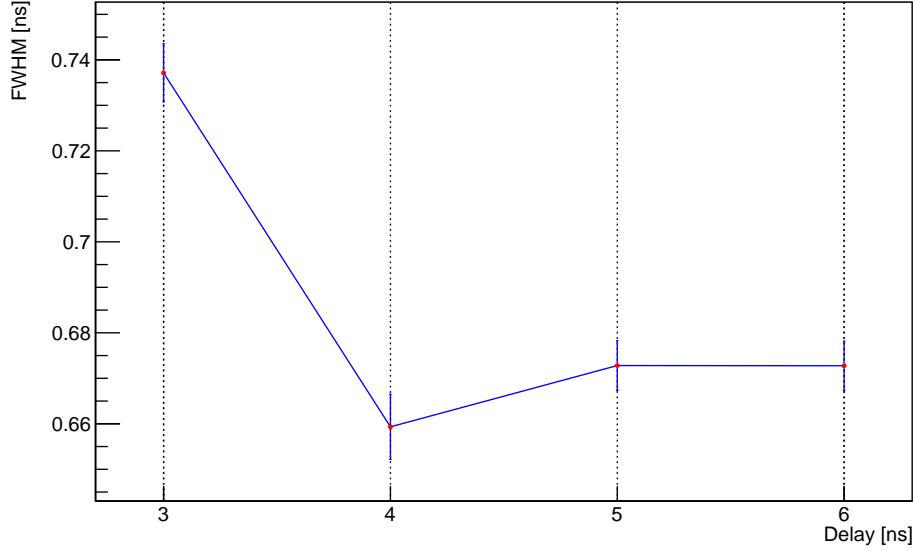


Figure 9: FWHM as a function of CFD delay.

## Analog Time resolution as function of energy

In order to study the time resolution dependence as a function of energy a different radioactive source,  $^{60}\text{Co}$ , was used. This source is chosen because of its high energy Compton Edge ( $\approx 1$  MeV) that allows to study the energy dependence up to this value.

Two methods were used to characterize the timing resolution for different energies:

- Energy Windows
- Energy Thresholds

In the following sections they will be described and the obtained results discussed.

## Energy Windows

The analog timing distributions were produced selecting events inside energy windows of 100 keV width in the range 100 keV-1 MeV (see Fig. 10).

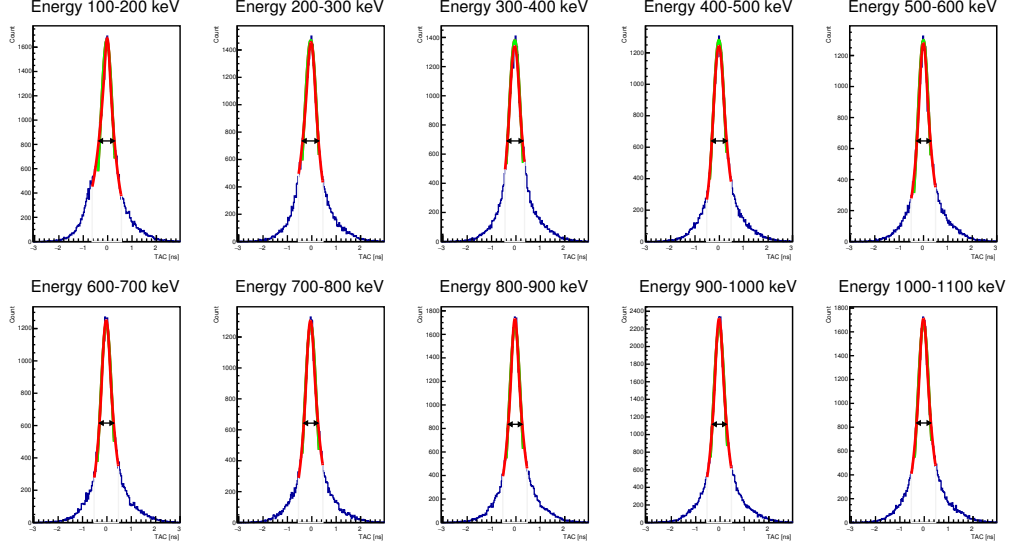


Figure 10: Timing distributions obtained selecting events inside 100 keV energy windows.

For each distribution the FWHM was computed and reported in the Fig. 11 below, over the 2-D density plot of timing as function of energy.

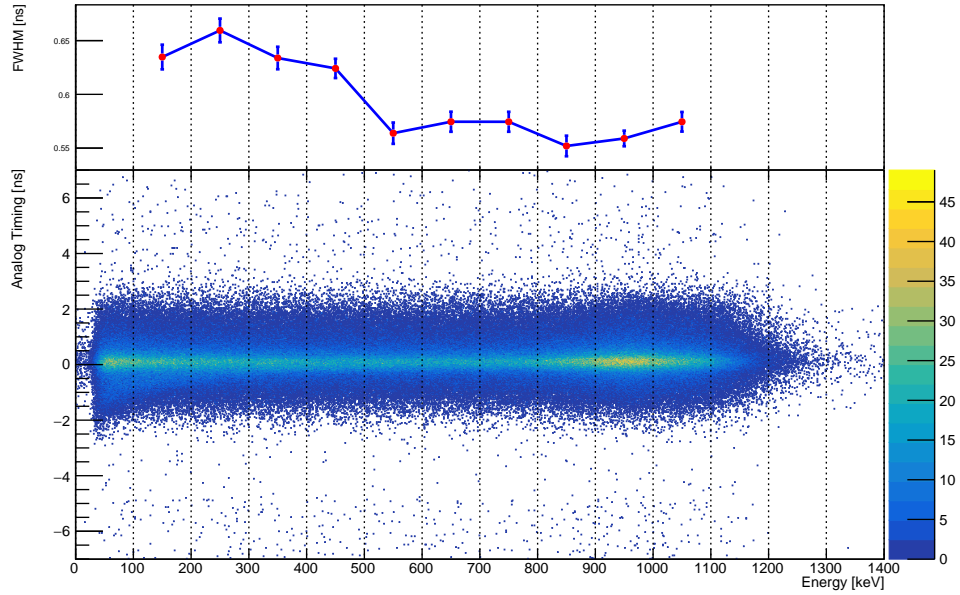


Figure 11: FWHM for each energy slice over 2-D density plot of timing as function of energy.



## Energy Threshold

The analog timing distributions were produced selecting events by mean of different energy thresholds from 100 keV to 1 MeV (see Fig. 12).

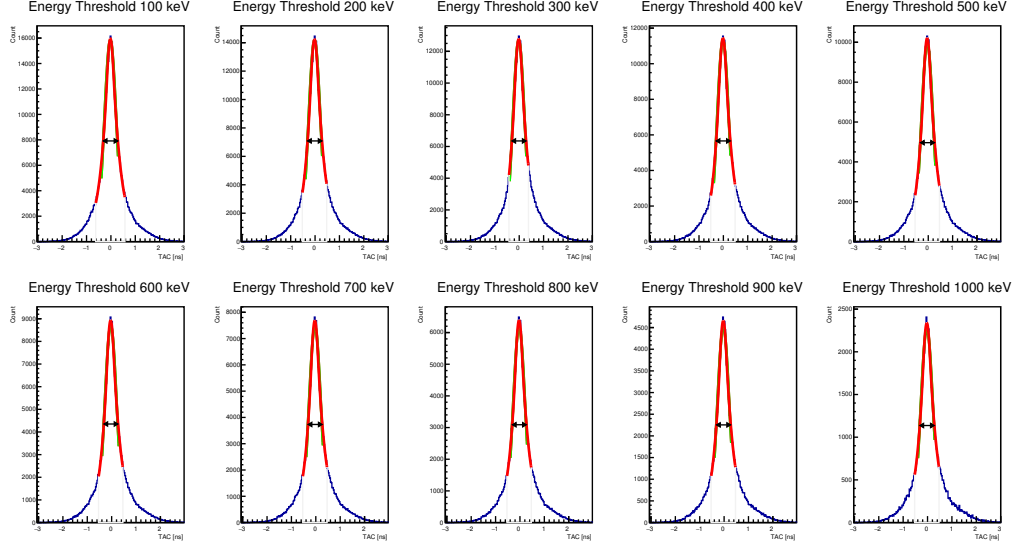


Figure 12: Timing distributions obtained selecting events by mean of different energy thresholds.

In the same way, for each distribution, the FWHM was computed and reported in the Fig. 13 below:

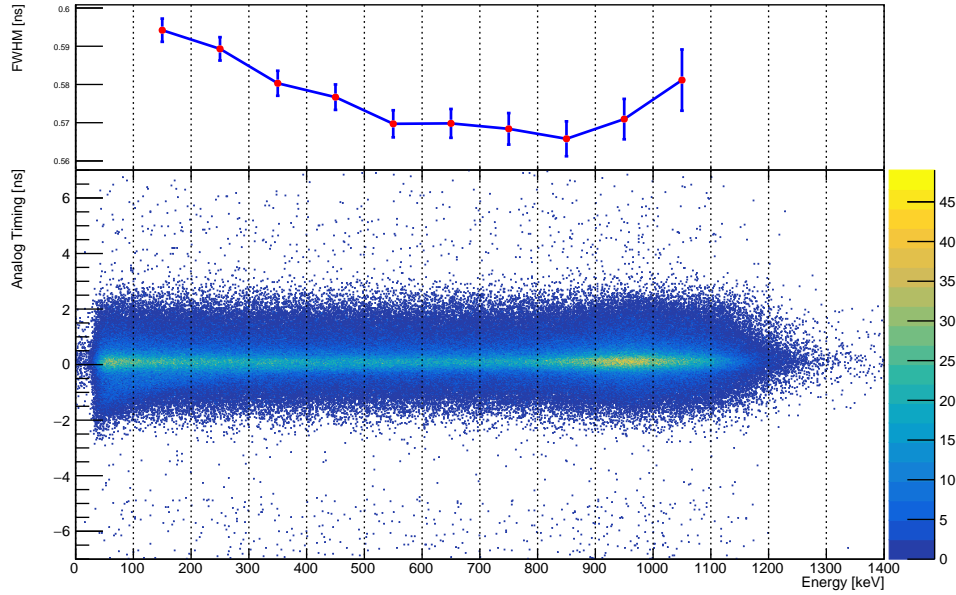


Figure 13: FWHM for each energy threshold over 2-D density plot of timing as function of energy..

## Methods comparison

The overlay of the FWHM obtained with the two methods is presented in Fig. 14. Both the curves show a minimum around the Compton edge of the spectrum, for greater energies the increasing of FWHM could be explained by mean of multi-scattering interactions inside the detectors.

The worst trend of the energy windows analysis is due by the less statistic of timing distributions with respect to threshold method. This is highlighted observing the FWHM associated errors, which decrease till the Compton edge, were the majority of signals occur. Differently, the opposite trend characterize the thresholds curve, because with increasing energies less events are collected.

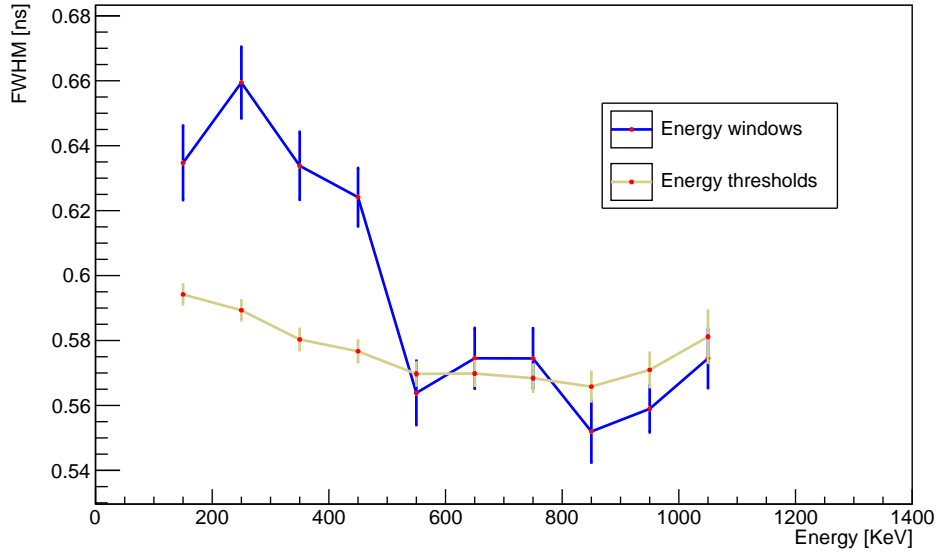


Figure 14: FWHM obtained from different energy windows and different energy thresholds compared.

## Digital Timing

Digital timing algorithm uses directly the digitized waveforms, performing a digital signal treatment similar to the analog one.

The CFD method works generating a bipolar signal from the original pulse and then computing its zero crossing as time reference. Lets name  $W_t$  the digitized waveform with  $t$  an integer number (sample number). The bipolar pulse  $P_t$  is calculated as:

$$P_t = \chi W_t - W_{t-\delta}, \quad (2)$$

where  $\chi$  is a reduction fraction and  $\delta$  an integer delay. Fig. 15 shows the CFD method applied on a signal.

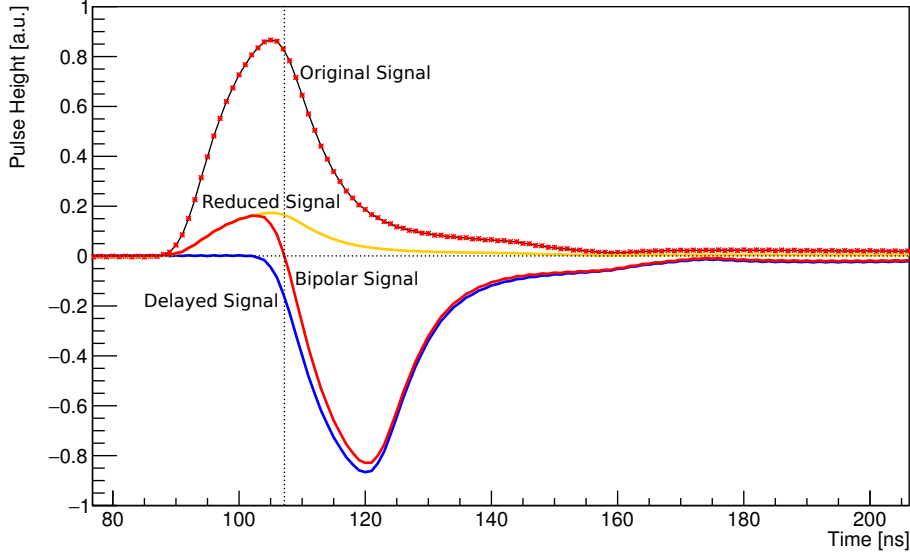


Figure 15: Digital waveform obtained as an average of  $10^4$  normalized signals. The Delayed and fractioned signals with their sum are represented too.

To increase the precision and reduce the dependence on the signal amplitude (time walk), the intersection with a zero crossing line is used. It is found by taking the samples above and below it and interpolating to find the time reference. A cubic spline interpolation with derivative bound continuity condition up to second order was chosen. Lets consider the sample range  $[t_{-1}, t_0]$  with  $t_0$  the first sampled point after the intersection and  $t_{-1}$  the preceding one. The reconstructed pulse  $f(t)$  inside the range is evaluated as follow:

$$f(t) = a(t - t_{-1})^3 + b(t - t_{-1})^2 + c(t - t_{-1}) + d$$

$$\begin{cases} a = 1/18(P_{t_{-3}} - 8P_{t_{-2}} + 19P_{t_{-1}} - 19P_{t_0} + 8P_{t_1} - P_{t_2}) \\ b = 1/30(-4P_{t_{-3}} + 32P_{t_{-2}} - 58P_{t_{-1}} + 37P_{t_0} - 8P_{t_1} + P_{t_2}) \\ c = 1/90(7P_{t_{-3}} - 56P_{t_{-2}} - 11P_{t_{-1}} + 74P_{t_0} - 16P_{t_1} + 2P_{t_2}) \\ d = P_{t_{-1}} \end{cases}$$

Similarly to the analog timing, an optimization of the CFD parameters was necessary. A first grid search was performed over several fractions and delays, selecting events inside a thin energy slice centered on the Compton edge. Fig. 16 shows the best parameters configuration with little delays and fractions. However these are not the right choice, with too low delay and fraction the bipolar signals formed would be too small and many events would be lost. This behavior is highlighted observing the density plot of the timing distribution integral inside the FWHM range shown in Fig. 17.

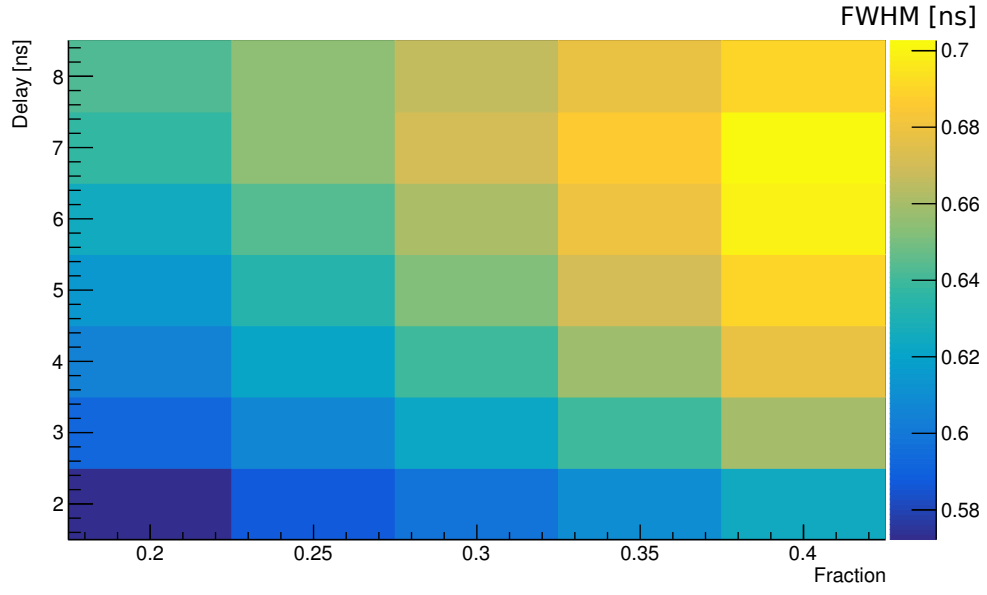


Figure 16: 2-D density plot of digital timing distribution FWHM obtained with different delays and fractions.

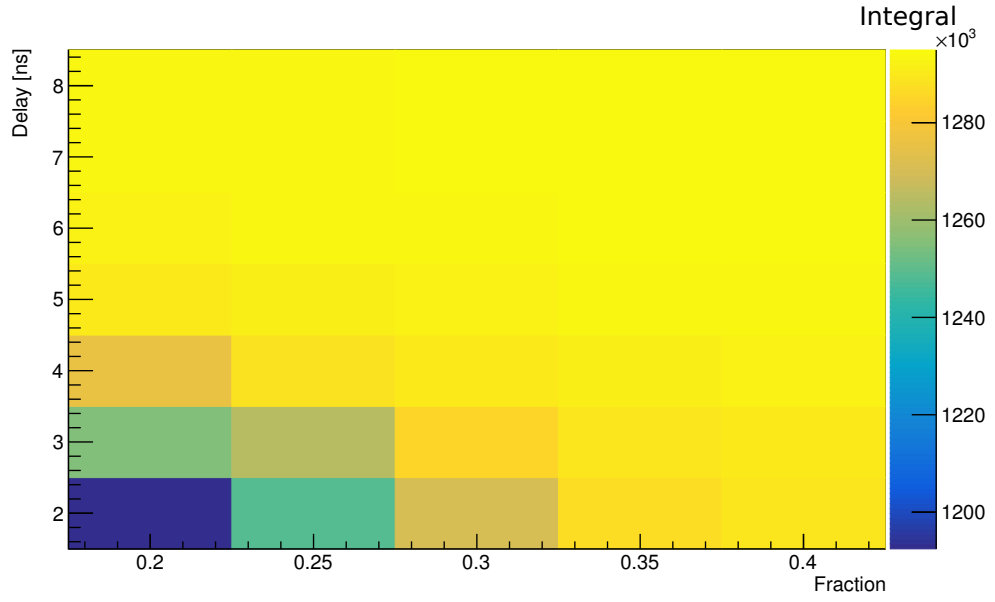


Figure 17: 2-D density plot of timing distribution integral inside the FWHM range, with different delays and fractions.

A new grid search was performed (see Fig. 18) finding the best resolution with:

$$\text{Fraction} = 0.16$$

$$\text{Delay} = 11 \text{ ns}$$

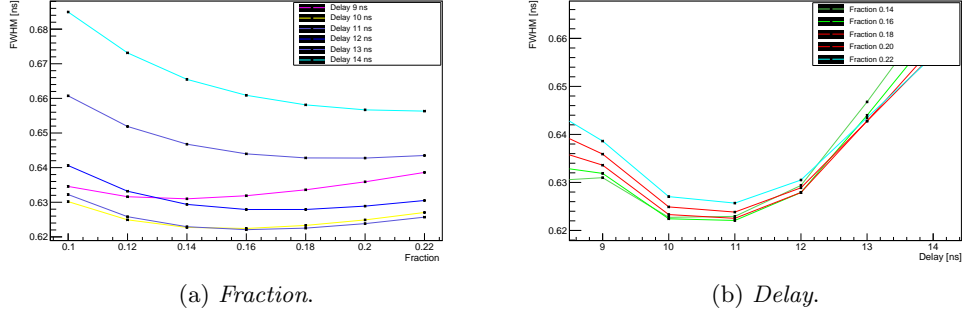


Figure 18: FWHM as a function of *Fraction* (a) and *Delay* (b). The different curves represent different value of the second parameter.

Using the selected fraction/delay configuration, the best zero crossing line value is computed in order to minimize the time walk. Fig. 19 shows the FWHM of timing distributions obtained from the whole energy spectrum from different zero crossing line values.

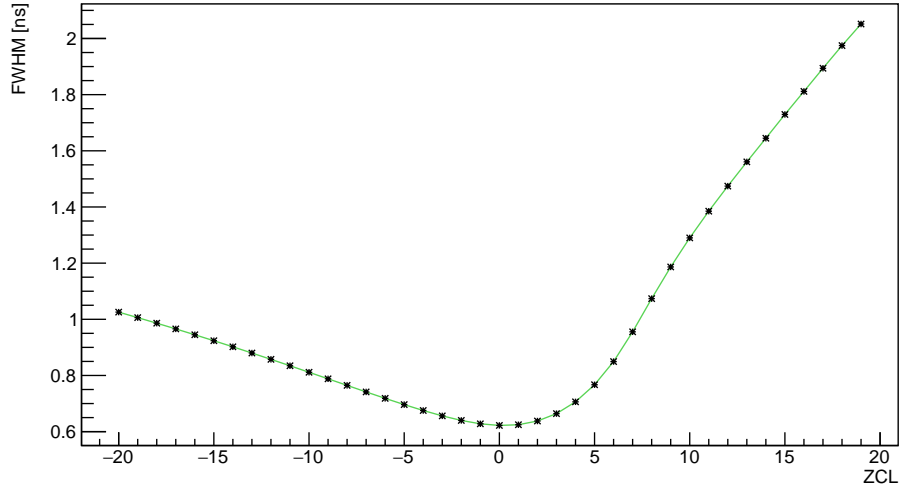


Figure 19: FWHM as a function of zero crossing line.

Finally, with the optimized parameters, was possible to perform the digital timing analysis. The  $^{22}\text{Na}$  source was used, similarly to the analog timing the FWHM of distributions obtained selecting events inside energy windows of 50 keV width were computed. Fig. 21 and Fig. 20 show respectively the distribution and the calculated FWHM for each energy windows.

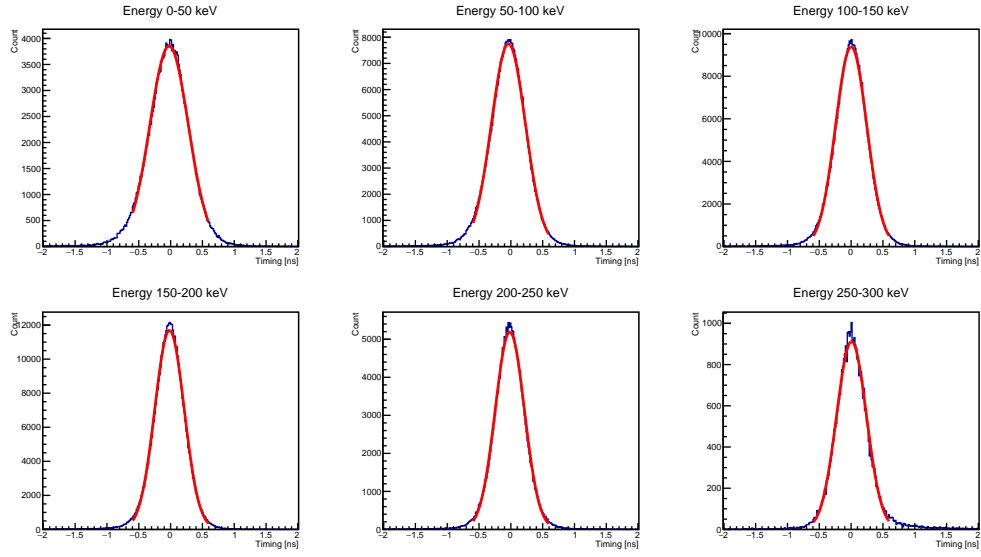


Figure 20: Digital timing distributions obtained selecting events inside 50 keV energy windows

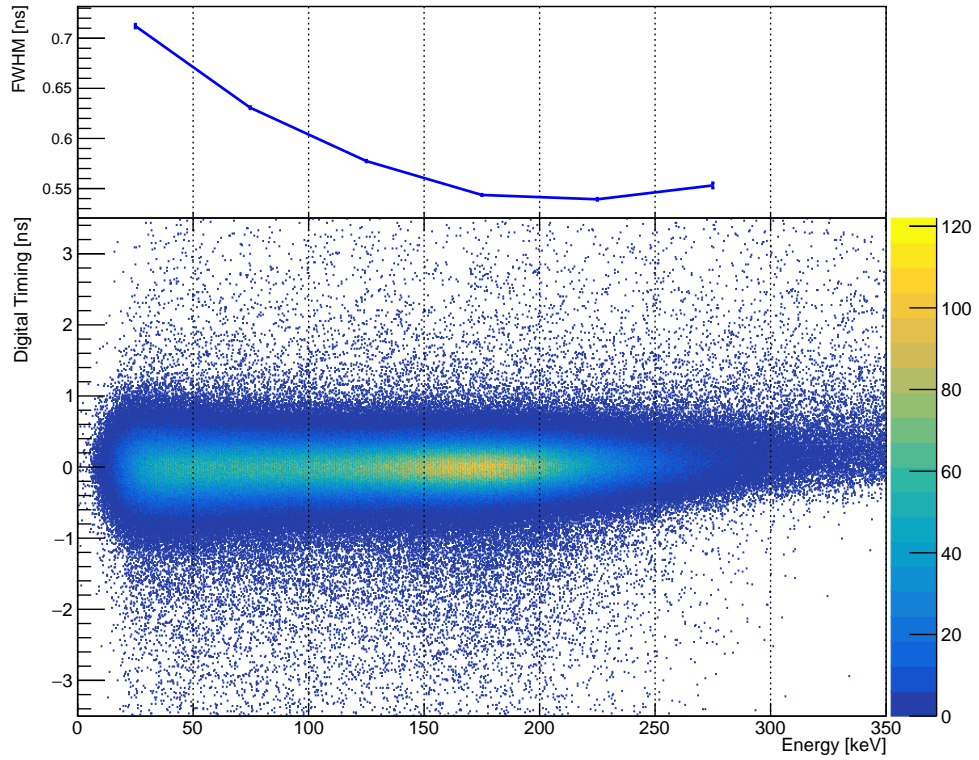


Figure 21: FWHM for each energy slice over 2-D density plot of digital timing as function of energy.

## Speed of light

In order to measure the speed of light, the  $\gamma$  source was moved between the two detectors. The position of the source ( $x$ ) with respect to the detectors was considered as shown in Fig. 22.

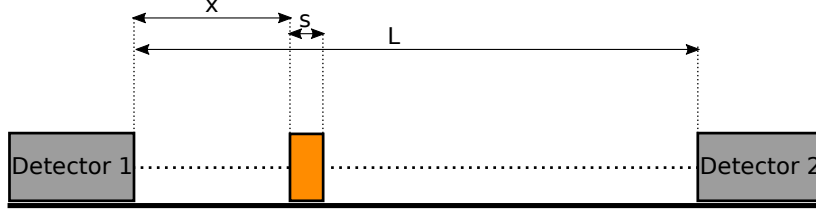


Figure 22: Source position between the detectors.

Considering the two coincident  $\gamma$  emission at  $t = 0$  the signals produced by the detectors will have the following timing reference:

$$T_1 = \frac{x + s/2}{c} + \delta_1$$

$$T_2 = \frac{L - x - s/2}{c} + \delta_2$$

where  $\delta_1$  and  $\delta_2$  are the constant cable delays of the electronic setup. Therefore the TAC will show the time value:

$$T_{\text{TAC}} = T_1 - T_2 = \frac{2x}{c} + \text{const.}$$

Using four different  $x$  positions the TAC distribution of Fig. 23 were produced.

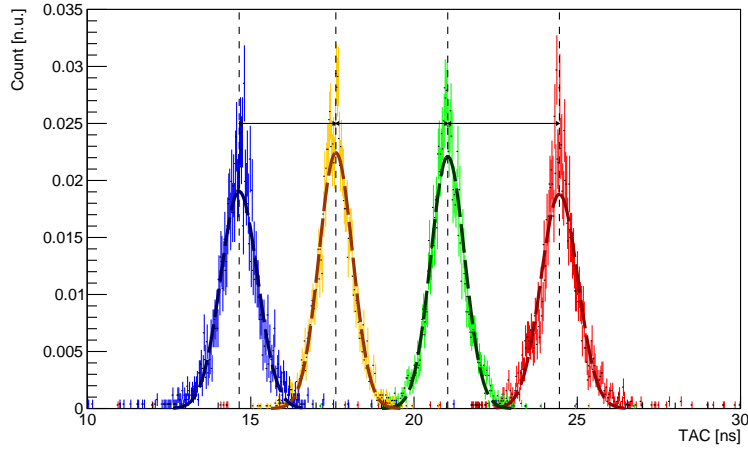
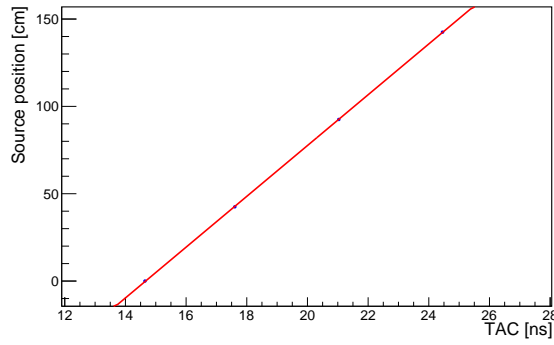


Figure 23: TAC distribution obtained in the four different  $x$  positions.

Computing the centroids of the peaks it was possible to draw  $x$  as a function of  $T_{\text{TAC}}$  as shown in Fig. 24 and perform a linear fit where the angular coefficient corresponds to  $c/2$ .



Parameter	Value
p0	$(-2.133 \pm 0.006) \times 10^2$ cm
p1	$14.54 \pm 0.03$ cm/ns
c	$29.08 \pm 0.06$ cm/ns

Figure 24: Linear Fit of  $x$  position as a function of  $T_{\text{TAC}}$  . Fit parameters and computed speed of light.

## Conclusion

The aim of this report was to describe the timing analysis performed over two scintillation detectors. Therefore the calibration and the electronic setup have been described. The timing analysis was produced using both analog and digital techniques, using  $^{22}\text{Na}$  and  $^{60}\text{Co}$  as  $\gamma$ -sources. The analog timing was produced using a Quad CFD mod. 935 and an Ortec TAC unit, and it allows to reach a FWHM of  $0.55 \pm 0.01$  ns in the range 700-800 keV. The digital timing was produced instead using a CFD algorithm over the digitized signals of the detectors. The FWHM reached is  $0.539 \pm 0.001$  ns in the range 200-250 keV.

Finally moving the source between the detectors was possible to compute an evaluation of the speed of light. The obtained value is  $29.08 \pm 0.06$  cm/ns.